Atmospheric Research 248 (2021) 105203

Contents lists available at ScienceDirect

Atmospheric Research

journal homepage: www.elsevier.com/locate/atmosres

Evaluating intensity-duration-frequency (IDF) curves of satellite-based precipitation datasets in Peninsular Malaysia

Muhammad Noor[a], Tarmizi Ismail[a], Shamsuddin Shahid[a,b,*], Md Asaduzzaman[c], Ashraf Dewan[d]

[a] School of Civil Engineering, Faculty of Engineering, Universiti Teknologi Malaysia (UTM), Johor Bahru 81310, Malaysia
[b] Centre for Coastal and Ocean Engineering (COEI), Universiti Teknologi Malaysia (UTM), Johor Bahru 81310, Malaysia
[c] Department of Engineering & Design, Staffordshire University, Stoke-on-Trent ST4 2DE, UK
[d] Spatial Sciences Discipline, School of Earth and Planetary Sciences, Curtin University, Perth, WA 6102, Australia

ARTICLE INFO

Keywords:
IDF curves
Remote sensing precipitation products
Probability distribution function
Ungauged location
Bias correction

ABSTRACT

In recent years the use of remotely sensed precipitation products in hydrological studies has become increasingly common. The capability of the products in producing rainfall intensity-duration-frequency (IDF) relationships, however, has not been examined in any great detail. The performance of four remote-sensing-based gridded rainfall data processing algorithms (GSMaP_NRT, GSMaP_GC, PERSIANN and TRMM_3B42V7) was evaluated to determine the ability to generate reliable IDF curves. The work was undertaken in Peninsular Malaysia. The best-fitted probability distribution functions (PDFs) of rainfall totals for different durations were used to generate the IDF curves. The accuracy of the gridded IDF curves was evaluated by comparing observed versus estimated IDF curves at 80 locations. The results revealed that a generalized extreme value (GEV) distribution had the best fit to the rainfall intensity for different durations at 62% of the stations, and this was then used to develop the IDF curves. A comparison of these remote sensing derived IDF curves with the observed IDF data revealed that the GSMaP_GC product performed best. In general, the satellite-based precipitation products tended to underestimate the IDF curves. The GSMaP_GC IDF curves were found to be the least biased (8%–27%) compared to the TRMM_3B42V7 IDF curves (65%–67%). The biases in rainfall intensity of different return periods for GSMaP_GC for all grid points were estimated. These results can be used in designing hydraulic structures where gauged data are unavailable.

1. Introduction

The changing nature of the earth's climate is now widely recognised. One result of this climate change is that the water holding capacity of the atmosphere is likely to increase (Trenberth, 2011). This has serious implications for the distribution of global precipitation (IPCC, 2014). Changes in extreme rainfall events will occur due to increased evaporation and atmospheric moisture content (Wang et al., 2016, Abbaspour et al., 2015; Pour et al., 2020a). Since rainfall is the major element of the hydrological cycle, any additional change in its distribution and volume may result in large scale flooding (Pour et al., 2014; Hajani et al., 2017; Pour et al., 2020b), resulting in significant damage to infrastructures such as dams, stormwater drainage systems (Shahid et al., 2017; Almazroui et al., 2019).

Global intensity-duration-frequency (IDF) curves are typically used to incorporate hydrological information into water infrastructures design (Watt and Marsalek, 2013; Koutsoyiannis et al., 1998; Şen, 2019). Such curves are based on the relationships between the frequency, intensity and duration of rainfall data (Koutsoyiannis et al., 1998), and the use of probability distribution functions (PDFs) of maximum rainfall depth (for a specific duration). This enables a relationship to be defined between the properties of a specific rainfall episode and the likelihood of rainfall totals (Chow et al., 1988). IDF curves can therefore be used to estimate probable extreme rainfall totals over differing durations and intensities. A number of studies have employed these IDF curves, utilising data from: a) in-situ rain-gauge (Willems, 2000; De Paola et al., 2014; Al-Amri and Subyani, 2017; Noor et al., 2019) remote sensing rainfall products (Endreny and Imbeah, 2009; Liew et al., 2014; Ombadi et al., 2018; Courty et al., 2019); both at local and global scales.

Traditionally ground-based rain gauge data has been used to construct IDF curves. Unfortunately a lack of consistent rainfall records at high temporal resolutions (hourly or sub-hourly) and a spatial sparseness of weather stations in many locations, are major barriers to the

* Corresponding author at: School of Civil Engineering, Faculty of Engineering, Universiti Teknologi Malaysia (UTM), Johor Bahru 81310, Malaysia.
E-mail addresses: tarmiziismail@utm.my (T. Ismail), sshahid@utm.my, hpsahar@utm.my (S. Shahid), md.asaduzzaman@staffs.ac.uk (M. Asaduzzaman), a.dewan@curtin.edu.au (A. Dewan).

https://doi.org/10.1016/j.atmosres.2020.105203
Received 27 April 2020; Received in revised form 16 August 2020; Accepted 18 August 2020
Available online 20 August 2020
0169-8095/

successful generation of IDF curves, particularly in countries where data is scarce Nashwan and Shahid, 2019a, Prein and Gobiet, 2017, Nashwan et al., 2018). As the spatial nature of IDF curves vary widely due to variations in the pattern of rainfall intensity and duration (Kidd et al., 2017; Sorooshian et al., 2011), it is common to use data from nearby recording stations to generate IDFs. This, however, may not be an ideal solution when used in the design of water infrastructure as it has been found that the accuracy of IDF curves tends to decrease significantly with distance from rain gauge locations (). To overcome the difficulties associated with sparse observational records, alternative data source is suggested to tackle engineering challenges (Courty et al., 2019), induced by climate warming (Liew et al., 2014).

A range of global, gridded precipitation products are now available which may be categorized as gauge-based (Herrera et al., 2012; Schiemann et al., 2010; Yatagai et al., 2009; Faiz et al., 2018), remote sensing-based (Nashwan and Shahid, 2019b; Huang et al., 2018; Palomino-Ángel et al., 2019; Almazroui and Saeed, 2020), reanalysis-based (Belo-Pereira et al., 2011; Yao et al., 2020), as well as a combination of the above three (Alijanian et al., 2017; Laiti et al., 2018). Because their spatial and temporal (hourly or sub-hourly) resolution is reasoanbly high, remotely sensed data products are particularly useful in developing IDF curves for hydro-climatic studies conducted at ungauged and data-sparse locations (Yang et al., 2014; Prakash et al., 2015; Belo-Pereira et al., 2011; Herrera et al., 2012; Schiemann et al., 2010; Yatagai et al., 2009; Nashwan and Shahid, 2019b). Furthermore, gridded precipitation data can assimilate the variability and dynamics of extreme rainfall events at ungauged locations which cannot be captured by rain gauges, and can thus help in overcoming issues related to the interpolation of point data (Chen et al., 2013; Marra et al., 2016; Panziera et al., 2016). The use of remotely sensed precipitation products in hydrological studies is, therefore, an area of increasing research focus.

Despite extensive use of gridded precipitation products obtained from satellite observation, such as stream flow simulation (Kumar and Lakshmi, 2018), flood modelling (Yuan et al., 2019; Nashwan et al., 2019), aridity assessment (Hasan et al., 2019), statistical structure of rainfall behaviour (Dewan et al., 2019), drought observation (Jiang et al., 2017; Yang et al., 2018), only a handful works have been conducted to date in developing IDF curves in different regions. This includes areas of the United States (Wright et al., 2013; Ombadi et al., 2018), eastern Mediterranean region (), Netherlands (Overeem et al., 2009) and Ghana (Endreny and Imbeah, 2009) and nine different cities of the world (Courty et al., 2019). The studies that have used gridded precipitation products, either from satellite or reanalysis, have shown immense potential, particularly in locations where precipitation data is scarce. For example, Courty et al. (2019) developed a universal IDF formula at the global scale using ERA5 reanalysis data. (Ombadi et al., 2018) developed IDF curves over the USA using PERSIANN-CDR data. developed IDF curves for East Mediterranean regions using radar and satellite (CMORPH) rainfall. Endreny and Imbeah (2009) used TRMM and observed rainfall data to develop IDF curves in Ghana. These studies suggest that a potential issue could be the reliability of the satellite-derived rainfall products as this differs from place to place, depending on the calculation processes and specific weather conditions (Serrat-Capdevila et al., 2016; Tan and Duan, 2017; Chen and Li, 2016). As a result, IDF curves developed from gridded rainfall data tend to deviate from curves developed from the observed rainfall data (Peleg et al., 2018). An exact match between IDF curves is not possible when the curves have been generated using two different datasets – (i) gridded, precipitation-based curves, and (ii) gauged-based IDF curves (). Endreny and Imbeah (2009) also suggested that the combined use of the satellite and observed data could provide useful insights for generating the IDF curves. It is essential to find the best remote sensing data product in order to generate bias-free or least biased IDF curves, and to subsequently correct the bias of remote sensing based IDF curves prior to use in any hydraulic design work.

The IDF curves at sub-daily scale are of prime importance to design hydraulic structures (Lima et al., 2018). The urban catchments are sensitive to shorter rainfall events, and thus, the drainage system should be based on sub-daily IDF curves (Courty et al., 2019). The curves at sub-daily resolution are particularly useful for tropical regions where intense short-duration rainfall is very common (Tien Thanh and Dutto Aldo Remo, 2018). The current work aims to assess the ability of remotely sensed precipitation data to generate sub-daily IDF curves. Four remote sensing rainfall products, namely Global Satellite Mapping of Precipitation - Gauge Calibrated (GSMaP), Global Satellite Mapping of Precipitation - Near Real-Time (GSMaP_NRT), Precipitation Estimation from Remotely Sensed Information using Artificial Neural Networks (PERSIANN) and Tropical Rainfall Measuring Mission (TRMM) are used to generate sub-daily IDF curves in countries where such data is difficult to obtain.

2. Materials and methods

2.1. Study area

The study area is located in Peninsular Malaysia between latitudes 1.20° N and 6.80° N, and longitudes 100.10° E and 104.20° E (Fig. 1). The area annually records 2000–4000 mm of rain from 150 to 200 wet days due to the tropical, humid climate (Nashwan et al., 2018; Noor et al., 2019). Monsoon winds, complex land-sea interactions and mountainous topography control the spatial variation of rainfall in the region (Pour et al., 2020c). Extreme rainfall events usually occur during the northeast monsoon (November to March), although these rainfall events can also occur during the inter-monsoon period (September–October and March–April), particularly in the west of the Peninsula (Mayowa et al., 2015; Khan et al., 2019). The mean annual temperature in the study area ranges from 21 °C to 32 °C.

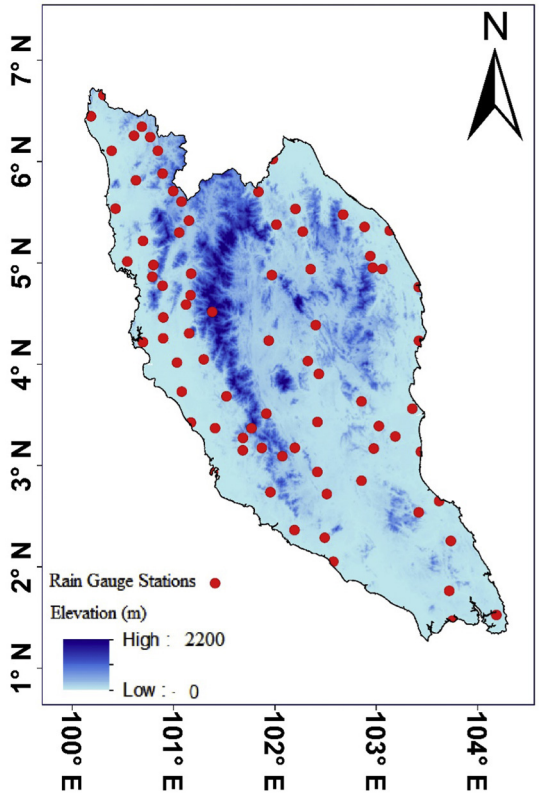

Fig. 1. Geographical boundary and topography of Peninsular Malaysia. Rain gauge stations used in this work are shown.

Table 1
Remote sensing precipitation datasets used in this study.

Data set	Temp resolution	Period	Pixel size	Source
GSMaP_NRT	1 h	2000–till	0.1 × 0.1	https://sharaku.eorc.jaxa.jp/GSMaP/index.htm
GSMaP_GC	1 h	2000–till	0.1 × 0.1	https://sharaku.eorc.jaxa.jp/GSMaP/index.htm
PERSIANN	3 h	2000–till	0.25 × 0.25	https://chrsdata.eng.uci.edu/
TRMM_3B42V7	3 h	1997–2019	0.25 × 0.25	https://pmm.nasa.gov/data-access/downloads/trmm

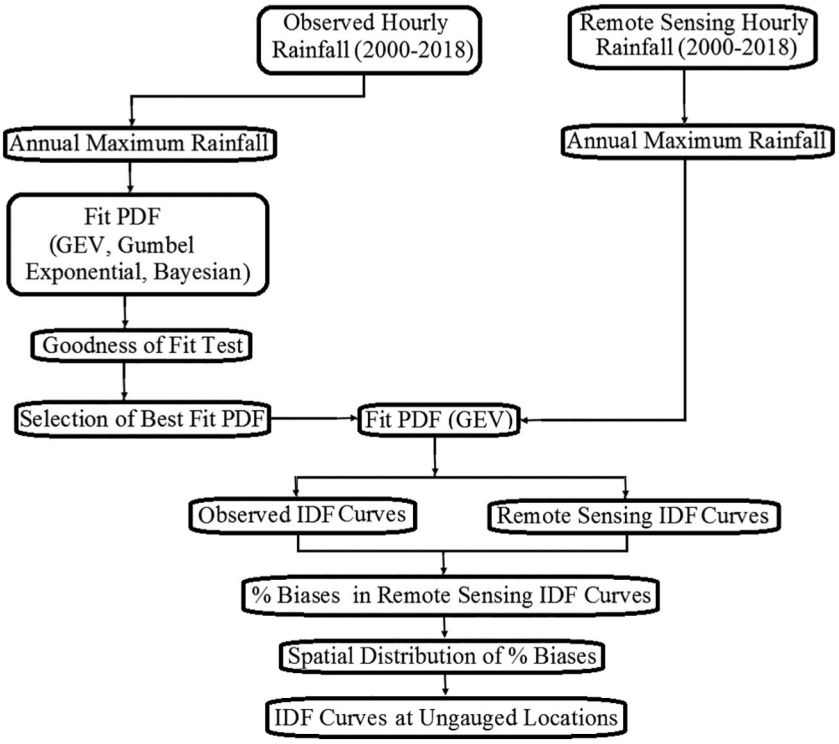

Fig. 2. Flowchart showing the development of IDF curves.

Table 2
Description of the statistical metrics used for evaluation of remote sensing data.

Metric formula	Range	Optimal value
$NRMSE = 100 * \frac{\sqrt{\frac{1}{n} * \sum_{i=1}^{n}(y_i - x_i)^2}}{sdv(x_i)}$	0 to ∞	0
$PBIAS = 100 * \frac{\sum_{i=1}^{N}(y_i - x_i)}{x_i}$	-∞ to + ∞	0
$md = 1 - \frac{\sum_{i=1}^{n}(x_i - y_i)^j}{\sum_{i=1}^{n}(\lvert y_i - \bar{x}\rvert + \lvert x_i - \bar{x}\rvert)^j}$	0 to 1	1
$rSD = \frac{sd(x_i)}{sd(y_i)}$	0 to ∞	1
$KGE = 1 - \sqrt{(r-1)^2 + (\gamma - 1)^2 + (\beta - 1)^2}$	−1 to -∞	1

where n is the samples number; x_i and $y_i$refer to the observed and remote sensing data, respectively for time step i; sd is the standard deviation; $\bar{x}$ and $\bar{y}$ are the mean of the observed and remote sensing data, respectively. r is Pearson's correlation of the remote sensing data (y) and observed data (x), γ represents the bias which is normalized by the standard deviation of the observed data, and β is a fraction of the coefficient of variation representing spatial variability.

2.2. Observed rainfall data

Hourly rainfall data from the 80 rain gauge stations distributed across the Peninsula were obtained from the Department of Irrigation and Drainage (DID), Malaysia. Locations of these stations are shown in Fig. 1. A common period of data for observed rainfall and satellite-based products (2000–2018) was used.

DID uses a standardised procedure for the measurement and archiving of rainfall data. In previous hydro-climatic studies conducted in this area, the quality of the DID rainfall data was found to be fit-for-purpose (Mayowa et al., 2015), however as part of the normal due diligence process, the quality of the rainfall data to be used in the current study was evaluated prior to processing using both subjective and objective evaluation methods. DID has 199 rain gauges available to record rainfall in Peninsular Malaysia. Data from 80 stations missing less than 1% of the hourly data for the 2000 to 2018 period were selected. Checks included looking for an absence of negative values, presence of hourly rainfall figures showing more than 50 mm, and one-day cumulative rainfall figures of more than 200 mm. Hourly, daily and monthly rainfall time series and histogram plots were prepared to find any irregularity in the dataset (Ahmed et al., 2019). Hourly and daily average values over a day and a year respectively were prepared to evaluate the consistency of the data. Data quality was also assessed using sequential student *t*-tests. All the rainfall data was deemed to be of adequate quality for the work and no abnormalities in the plots was noted. No significant differences among the different subsets of data was noted using the t-test.

2.2.1. Remote sensing precipitation data

Four remotely sensed precipitation data products were acquired and evaluated in the present study (Table 1). The GSMaP precipitation product is collected and compiled by Core Research for Evolutional Science and Technology (CREST) of the Japan Science and Technology

Table 2
Results of goodness-of-fit test for different probability distribution functions and parameter estimation methods for rainfall amounts of differing duration at a location in Southern Malaysia (station Johor 2,025,001).

Estimator	Distribution	Duration (hours)						
		1	3	6	12	24	48	72
MLE	GEV	175.25	194.05	199.39	202.48	206.24	216.27	217.67
	Gumbel	279.44	299.13	304.49	307.05	309.87	322.57	323.93
	Exp	222.61	238.37	241.84	244.98	249.55	257.89	263.14
	GP	296.27	330.07	343.16	354.56	374.85	358.47	356.47
GMLE	GEV	185.62	197.89	203.30	204.28	212.53	219.23	222.62
	Gumbel	279.44	299.13	304.49	307.05	309.87	322.57	323.93
	Exp	222.61	238.37	241.84	244.98	249.55	257.89	263.14
	GP	487.07	495.39	493.95	496.71	498.34	478.35	491.01
L-Moments	GEV	440.55	669.89	733.69	808.03	744.84	817.29	882.53
	Gumbel	∞	∞	∞	∞	∞	∞	∞
	Exp	∞	∞	∞	∞	∞	∞	∞
	GP	487.07	495.39	493.95	496.71	498.34	478.35	491.01
Bayesian	GEV	436.67	669.32	763.45	753.54	703.70	777.73	793.23
	Gumbel	∞	∞	∞	∞	∞	∞	∞
	Exp	∞	∞	∞	∞	∞	∞	∞
	GP	∞	∞	∞	∞	∞	∞	∞

Agency (JSTA) in collaboration with the Japan Aerospace Exploration Agency (JAXA) Precipitation Measuring Mission (PMM) Science Team (Okamoto et al., 2005; Ushio et al., 2009). It comprises two products - (i) GSMaP_NRT, developed by integrating global precipitation rates extracted from passive microwave radiometers and cloud moving vectors derived from infrared images, and (ii) GSMaP_GC, which is an adjusted product of GSMaP_NRT using the NOAA Climate Prediction Center (CPC) precipitation data (Nashwan and Shahid, 2019b). PERSIANN is precipitation estimated from geostationary satellite-based infrared brightness temperature using a neural network function (Nguyen et al., 2018). It is produced by the Center for Hydrometeorology and Remote Sensing (CHRS) at the University of California, Irvine (UCI). Tropical Rainfall Measuring Mission (TRMM) data is a joint mission between JAXA and NASA (Huffman, 2016). In this study, 3 h real time TRMM multi-satellite precipitation analysis information (TRMM_3B42V7) (Mission, 2011) is used.

3. Methodology

3.1. General IDF relationship for different distributions

The intensity-duration-frequency (IDF) relationship is a popular method that relates rainfall intensity with its duration and annual frequency. For a given duration d, return period T and the maximum intensity $i(d,T)$ of rainfall at a specific location, the general form of the intensity-duration-frequency (IDF) curve (Koutsoyiannis et al., 1998) can be formulated as:

$$i(d,T) = a(d,T)\cdot(d+\theta)^{-\eta} \tag{1}$$

where $a(d,T)$ and $i(d,T)$ are functions of d and T, θ and η are parameters with $\theta > 0$ and $1 < \eta < 0$. Koutsoyiannis et al. (1998) established the relationship between the cumulative distribution function (CDF) of the maximum intensity and the return period T given as:

$$a(d,T) = F_Y(y_T) = 1 - \frac{1}{T} \tag{2}$$

The IDF relationship (Koutsoyiannis et al., 1998) between the maximum amounts of rainfall with distribution function $F_Y(\cdot)$ with T for d is, therefore, presented as:

$$y_T = a(d,T) = F_Y^{-1}(1 - 1/T) \tag{3}$$

In this study, we consider four widely used probability distributions to fit IDF curves and evaluate the individual performances. These are Exponential, Generalized Pareto (GP), Gumbel and Generalized Extreme Value (GEV). The exponential distribution is a fundamental distribution for establishing several other distributions. The exponential distribution function is broadly applied in hydrological studies (Kjeldsen et al., 2000). This distribution has applicability in such things as the frequency analysis of rainfall amount and extreme events (Zhu et al., 2019). The PDF of the exponential random variable is given by:

$$F(y) = \begin{cases} 1 - \exp\left(-\frac{y}{\lambda} + \psi\right), x \geq 0 \\ 0, \quad otherwise \end{cases} \tag{4}$$

where λ and ψ are the scale and location parameters respectively. The IDF relationship for the exponential distribution (Koutsoyiannis et al., 1998) can be expressed as:

$$y_T \equiv a(T) = \lambda(\psi + \ln T) \tag{5}$$

Pikands (1975) suggested the Generalized Pareto (GP) distribution, which has been applied in the various fields. GP distribution plays a significant role in modelling of extreme events e.g., the analysis of the highest annual flood values, the precipitation data analysis, in the analysis of flood frequency, etc. The PDF of generalized pareto distribution is expressed as:

$$F(y) = 1 - \left[1 + k\left(\frac{y}{\lambda} - \psi\right)\right]^{-\frac{1}{k}}, y \geq \lambda\psi \tag{6}$$

where k is the shape parameter. For the GP distribution, the IDF relationship (Koutsoyiannis et al., 1998) is obtained as:

$$y_T \equiv a(T) = \lambda\left(\psi + \frac{T-1}{k}\right) \tag{7}$$

Gumbel distribution or Extreme Value Type I (EV1) distribution is often used in the frequency analysis of hydrological extremes e.g., floods, storms, wind speed, droughts, etc. (Yue and Wang, 2004; Hong et al., 2013). The PDF of Gumbel distribution can be given as:

$$F(y) = \exp\left(-\exp\left(\frac{-y}{\lambda} + \psi\right)\right) \tag{8}$$

The IDF relationship for Gumbel distribution (Koutsoyiannis et al., 1998) can be given by

$$y_T \equiv a(T) = \lambda\left(\psi - \ln\left[-\ln\left(1 - \frac{1}{T}\right)\right]\right) \tag{9}$$

The Generalized Extreme Value (GEV) distribution (developed within the extreme value theory) is a family of continuous probability

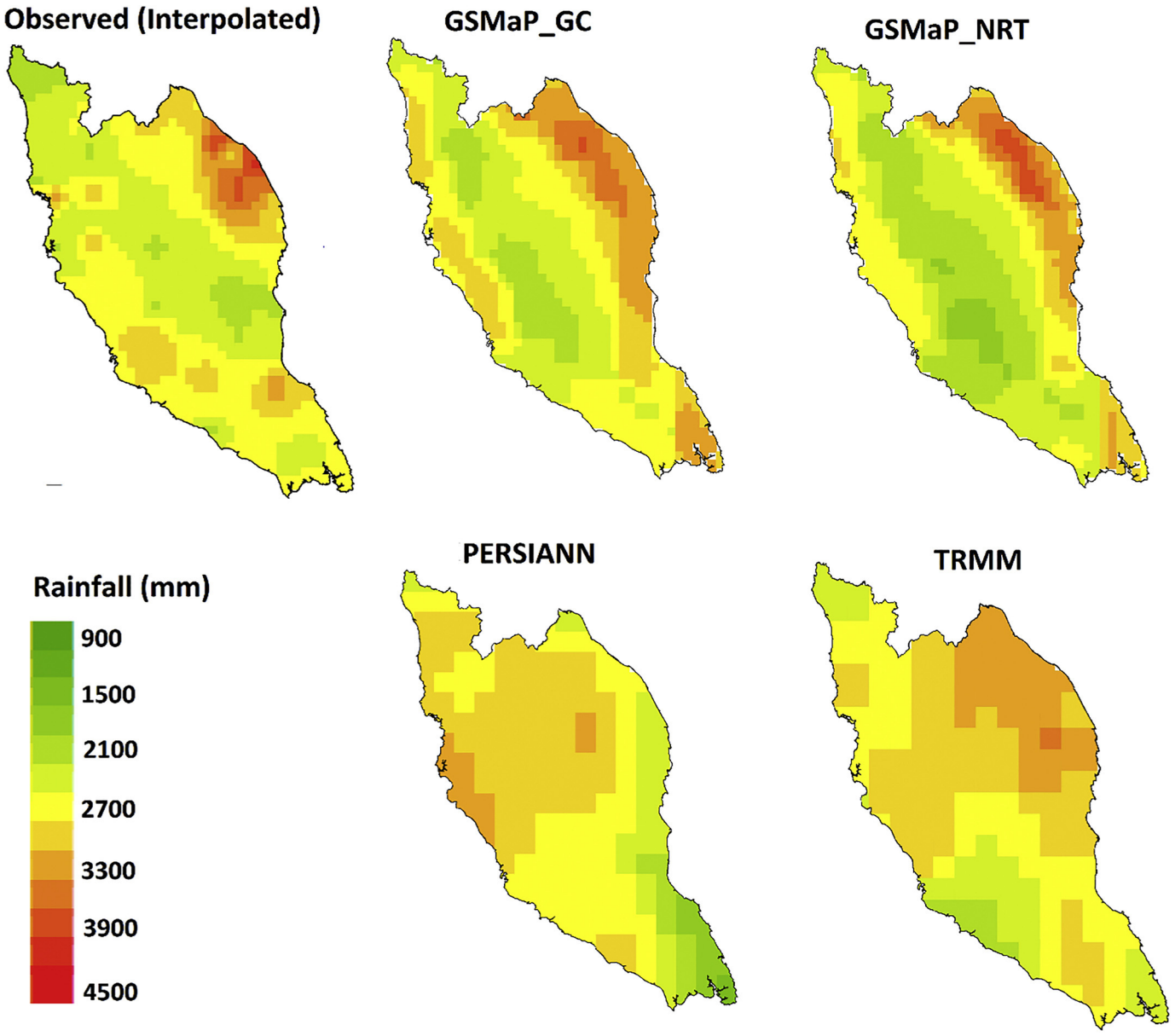

Fig. 3. Annual average rainfall in Peninsular Malaysia derived from observed and satellite data products for the period 2000–2018.

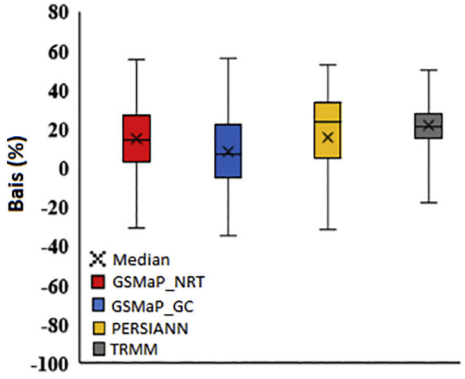

Fig. 4. Percent of bias in median of annual average of remotely sensed rainfall data.

distributions. The GEV distribution originated from the extreme value axiom and is the limit distribution of normalized maxima of an independent and identically distributed random variable. The PDF of the GEV is represented as (Jenkinson, 1955),

$$F(y) = \exp\left(-\left[1 + k\left(\frac{y}{\lambda} - \psi\right)\right]^{-1/k}\right), y \geq \lambda(\psi - 1/k) \tag{10}$$

Koutsoyiannis et al. (1998) established the IDF relationship for the GEV distribution can be given as:

$$y_T \equiv a(T) = \lambda\left(\psi + \frac{\left[-\ln\left(1 - \frac{1}{T}\right)\right]^{-k} - 1}{k}\right) \tag{11}$$

3.2. Estimation of parameters and fitting IDF curve

The Maximum Likelihood Estimation (MLE), Generalized Maximum Likelihood Estimation (GMLE), Bayesian and L-moments are commonly used methods for fitting PDFs for annual extreme rainfall time series data (Martins and Stedinger, 2000). In this study, performance of all the

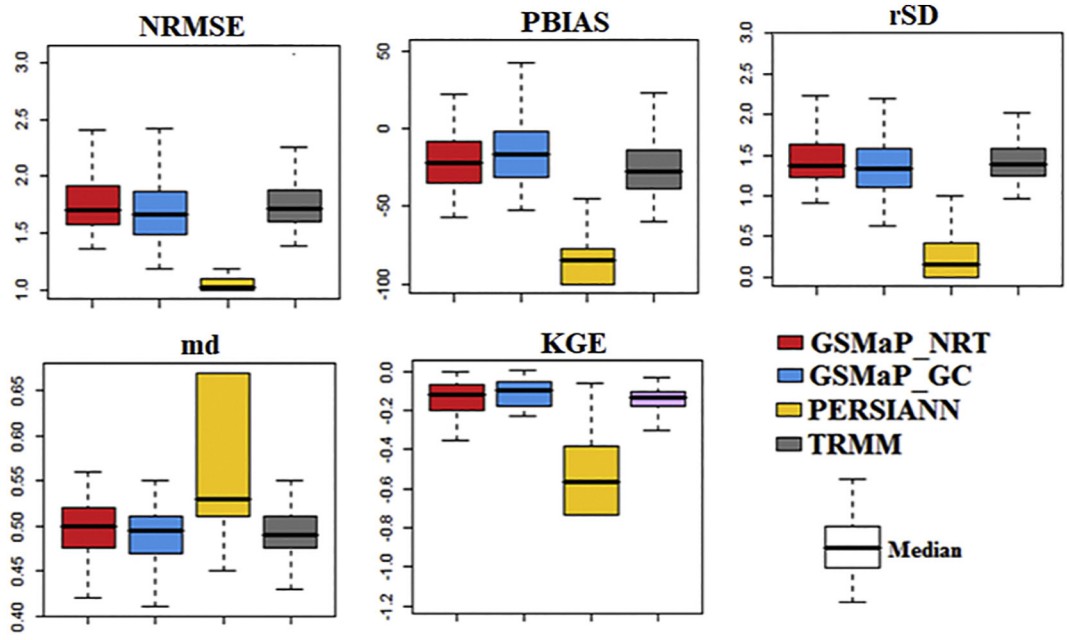

Fig. 5. A comparison of time series of remote sensing rainfall data with observed rainfall data at all the 80 observed locations.

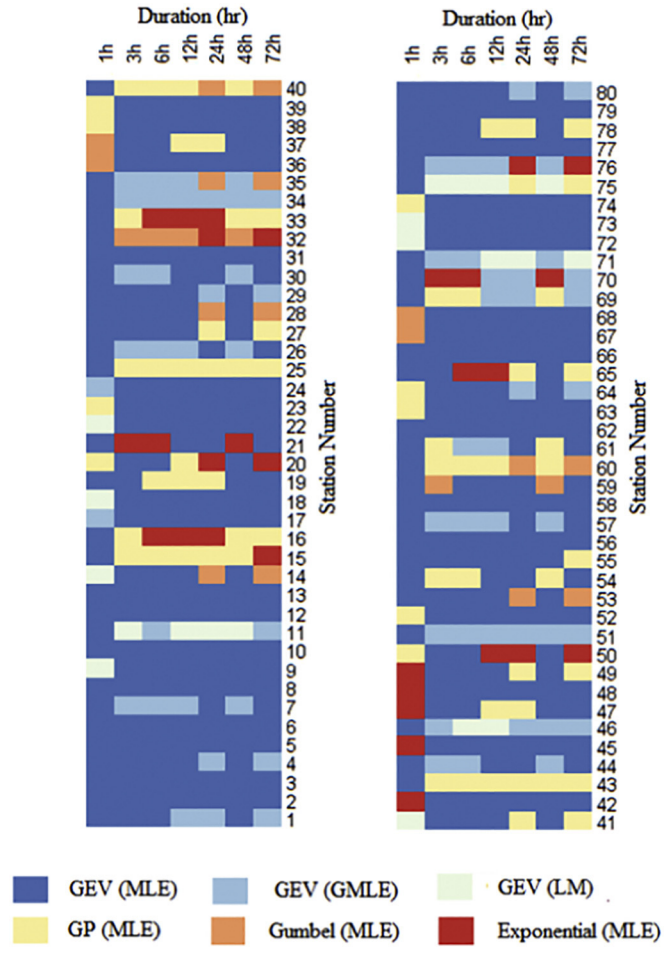

Fig. 6. Best fitted probability distribution function (PDF) for different rainfall periods and most suitable parameter estimation method.

four methods were compared to find the best parameter estimation method. Goodness-of-fit test was used as it is the best parameter estimation method. Several goodness-of-fit tests are available in the literature, but there are no general criteria for selecting a suitable test (Rahman et al., 2013). However, the log-likelihood approach, developed by R.A Fisher (Fisher, 1912), appears to be the most widely used for performance assessment of PDF (Fienberg, 1997; Zhu et al., 2018; Bierman et al., 1989; Poudel and Cao, 2013).

The likelihood is the joint density of n independent observations, $y = (y_1 \ldots . y_n)'$ which can be expressed as,

$$L(\theta) = f(y \mid \theta) = \prod_{i=1}^{n} f(y_i \mid \theta), \tag{12}$$

where $f(y|\theta)$ is the PDF and θ is the unknown parameter (Hilbe and Robinson, 2013). Often, natural logarithm of the likelihood function $L(\theta)$ is called the log-likelihood function ($LL(\theta)$), which is used to estimate parameters (instead of the likelihood function) due to mathematical tractability. Due to the monotonicity property, the estimates from the log-likelihood function $LL(\theta)$ also gives the same estimates by retaining all properties (Hilbe and Robinson, 2013). The $LL(\theta)$ is defined as.

$$LL(\theta) = \ln L(\theta) = \sum_{i=1}^{n} \log f(y_i \mid \theta) \Big) \tag{13}$$

For ease of computation, the negative logarithm of the likelihood estimates or the negative log-likelihood is commonly practised (Bosman and Thierens, 2000).

The GMLE estimates parameters in a similar manner to that used in the MLE method (Martins and Stedinger, 2000). Additional conditions eliminate the set of potential invalid values on some parameters while estimating the parameter of interest. This is done by setting initial distributions for those parameters (Martins and Stedinger, 2000). The GMLE involves solving the following optimization problem,

$$\begin{aligned} &\max_{\theta} L_n(x;\theta) \\ &\beta \sim \text{gamma}(u, v) \end{aligned} \tag{14}$$

where θ is the parameter of interest and β is the other parameter which follows a gamma prior distribution. The GMLE method is, therefore, analogous to the Bayes estimation method as it is equivalent to maximizing a posterior distribution. Since the posterior form is unknown, in general, numerical techniques like Markov chain Monte Carlo (MCMC)

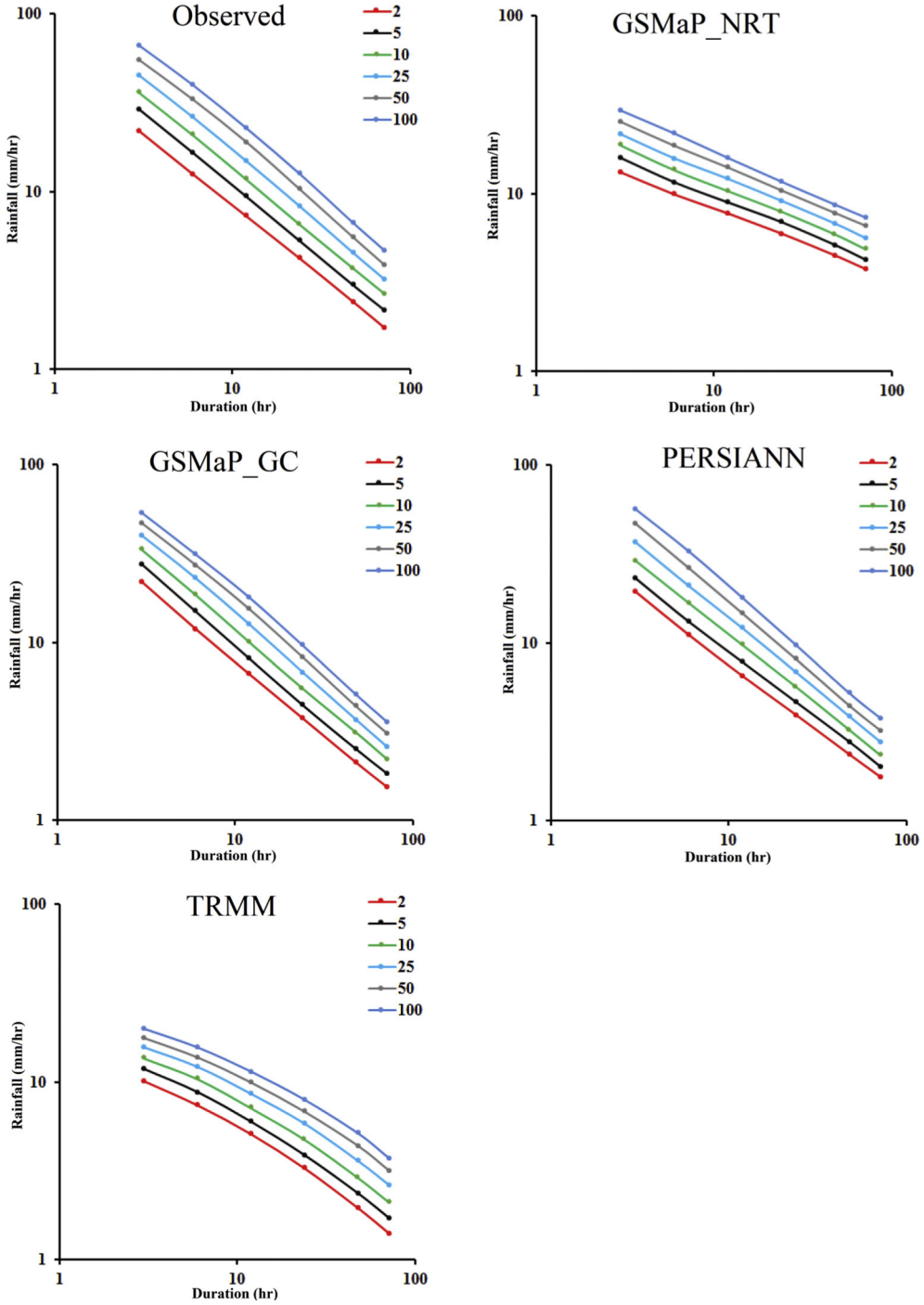

Fig. 7. IDF curves for Pahang station (ID: 3628001), showing suitable PDF and parameter estimate.

is applied to calculate parameters.

Bayesian method of parameter estimation involves specifying a prior probability density function, say $\pi(\theta)$ (Reis Jr and Stedinger, 2005). After the prior has been specified, the posterior distribution of θ is computed, and from this inferences can be made. Using Bayes Theorem, the conditional density of θ given data $y_1, y_2, \ldots, y_n$ is written as

$$\pi(\theta \mid y_1, y_2, \ldots, y_n) = \frac{f(y_1, y_2, \ldots, y_n \mid \theta)\,\pi(\theta)}{f(y_1, y_2, \ldots, y_n)} = \frac{[\Pi_i f(y_i \mid \theta)]\pi(\theta)}{\int_\Omega [\Pi_i f(y_i \mid \theta)]\,\pi(\theta)d\theta} \tag{15}$$

where Ω is the parameter space. *Re*-writing $\Pi_i f(y_i \mid \theta)$ as the likelihood function, $L(y_i \mid \theta)$, we get

$$\pi(\theta \mid y_1, y_2, \ldots, y_n) = \frac{L(y_i \mid \theta)\,\pi(\theta)}{\left(\int_\Omega L(y_i \mid \theta)\right)\pi(\theta)d\theta} \tag{16}$$

The posterior distribution is then maximized for the parameter values θ (Reis Jr and Stedinger, 2005).

Hosking (1990, 1990) proposed the L-moments method which is frequently used for the characterization of data, characteriztaion of PDFs, testing of PDF hypotheses and parameter estimation of PDFs. For a real valued ordered random variate Y of n samples, $y_{1:n} \le y_{2:n} \le \ldots \le y_{n:n}$ for cdf $F(y)$ and quantile function $y(F)$, the r-th L-moment of Y can be described as a linear function of the expected order statistics and can be represented as (Hosking, 1990)

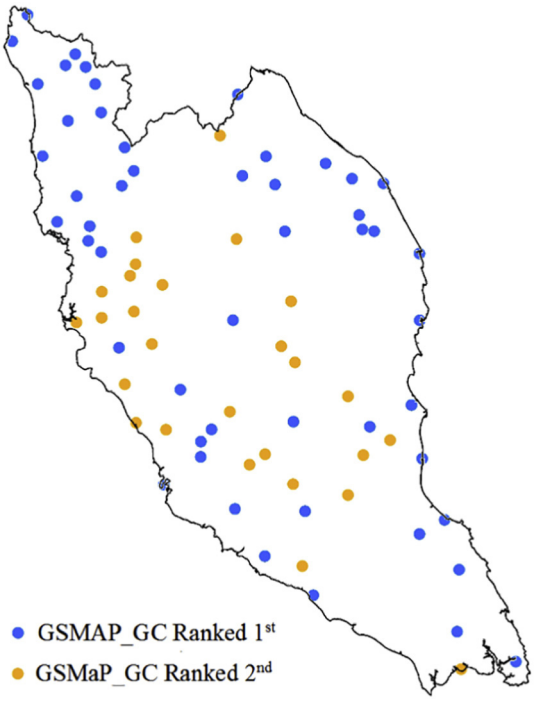

Fig. 8. Remote sensing precipitation product ranking in the replication of observed IDF curves at different rain gauge locations.

$$\lambda_r = \frac{1}{r}\sum_{k=0}^{r-1}(-1)^k\binom{r-1}{k}EY_{r-k:r},\ r = 1, 2, 3.... \tag{17}$$

The letter 'L' in 'L-moments' reveals the fact that r-th L-moment λ_r is a linear function of the expected order statistics. Furthermore, based on the oberved sample the natural estimate of the L-moment λ_r is the L-statistics. The probable value of order statistics can be represnted as:

$$E(Y_{j:r}) = \frac{r!}{(j-1)!(r-j)!}\int y[F(y)]^{j-1}[1-F(y)]^{r-j}dF(y) \tag{18}$$

The first four L-moments are derived as (Hosking, 2006):

$$\lambda_1 = E(Y) = \int_0^1 y(F)dF \tag{19}$$

$$\lambda_2 = \frac{1}{2}E(Y_{2:2} - Y_{1:2}) = \int_0^1 y(F)(2F-1)\,dF \tag{20}$$

$$\lambda_3 = \frac{1}{3}E(Y_{3:3} - 2Y_{2:3} + Y_{1:3}) = \int_0^1 y(F)(6F^2 - 6F + 1)\,dF \tag{21}$$

$$\lambda_4 = \frac{1}{4}E(Y_{4:4} - 3Y_{3:4} + 3Y_{2:4} - Y_{1:4}) = \int_0^1 y(F)(20F^3 - 3F^2 + 12F - 1)\,dF \tag{22}$$

3.3. Development of IDF curves

The process used for the development of the IDF curves is shown in Fig. 2. The parameters of best-fitted PDF are used to generate observed IDF curves, using hourly rainfall observations and remotely sensed-based rainfall IDF curves at 80 stations. They are developed by fitting the PDF to annual precipitation maximum data e.g. annual maximum of daily one-, two-, three-, or more hour rainfall amount. The parameter of the fitted PDFs is then applied to calculate the return period of maximum rainfall depth for each duration. The return periods of the rainfall intensities of corresponding durations are then plotted to prepare the IDF curves. In the present study, IDF curves are constructed for 2-, 5-, 10-, 2–5, 50- and 100-year return periods and 1-, 3-, 6-, 12-, 24-, 48- and 72 h rainfall durations.

3.4. Performance assessment

Two approaches can be used for comparing gridded rainfall data with in-situ rainfall: (i) in-situ rainfall is converted into gridded rainfall through interpolation, and then a grid-to-grid comparison is made; (ii) gridded data is interpolated to in-situ location and then compared with in-situ data (Nashwan et al., 2019; Ahmed et al., 2019; Pour et al., 2020d). In the present study, the second approach was used as the resolution of the remote sensing datasets differed. The satellite rainfall data of the four nearest grid points of an observed station were interpolated at the observed location using an inverse distance weighting method and then compared with the observed rainfall. Five statistical metrics were used to assess the performance of the remote sensing data - normalized root mean square error (*NRMSE*), percentage of bias (*PBIAS*), ratio of standard deviations (*rSD*), modified index of agreement (*md*) and Kling-Gupta Efficiency (*KGE*). The formulas, range and optimum values of the metrics are presented in Table 2. (See Table 2.)

4. Results and discussion

4.1. Performance of satellite-based rainfall data products

The annual average rainfall figures recorded at 80 rainfall gauges is interpolated to a resolution of 0.1° × 1° (the finest resolution of the remote sensing data used) using an inverse distance weighting technique to compare the spatial distribution of the observed and the remotely sensed rainfall (Fig. 3). The spatial distribution of GSMaP_NRT and GSMaP_GC rainfall appeared to have a better match with the spatial distribution of the observed rainfall than those of PERSIANN and TRMM. However, the GSMaP_NRT results were found to overestimate the annual rainfall at more grid points when compared to GSMaP_GC. PERSIANN and TRMM were found to underestimate the annual rainfall in the northeast high rainfall regions and overestimate the rainfall in most other areas.

The bias percent in the median value of the annual average of remotely sensed rainfall data is shown in the boxplots in Fig. 4. The results show an overestimation of rainfall by all the remote sensing precipitation data. The overestimation in median precipitation was 14.1% for GSMaP_NRT, 7.2% for GSMaP_GC, 23.9% for PERSIANN and 21.2% for TRMM_3B42V7. Overall, the results indicate a better performance by GSMaP_GC in replicating the spatial distribution of annual average Malaysian rainfall, with the least bias. However, the range of bias in GSMaP_GC at different grid points was higher than for the other precipitation products. This indicates a wide variation in the spatial performance of GSMaP_GC in Peninsular Malaysia.

Previous studies conducted on remote sensing precipitation products in the study area have also reported an overestimation of rainfall. Zad et al. (2018) looked at the performance of TRMM_3B42V7 in the Pahang river basin of Peninsular Malaysia and reported an overestimation of daily rainfall by TRMM at most locations. Tan et al., 2015 also reported an overestimation of rainfall by TRMM and PERSIANN-CDR. Giarno et al. (2018) evaluated the performance of TRMM satellite rainfall products over the Makassar Strait in Indonesia and also reported an overestimation of rainfall.

The time series of observed and remote sensing data at all 80 grid points were compared in order to evaluate the capability of remote sensing data to replicate the observed time series. The results are presented in Fig. 5. The GSMaP_GC indicated less NRMSE and PBIAS in comparison to the other products. Three other statistical metrics of GSMaP_GC were also found to be nearer to the optimum value when compared to other products. In construction, PERSIANN performed the worst of the four products in term of all statistical metrics.

Hur et al. (2018) compared the performance of TRMM and GSMaP_GC rainfall in Singapore and reported both products were

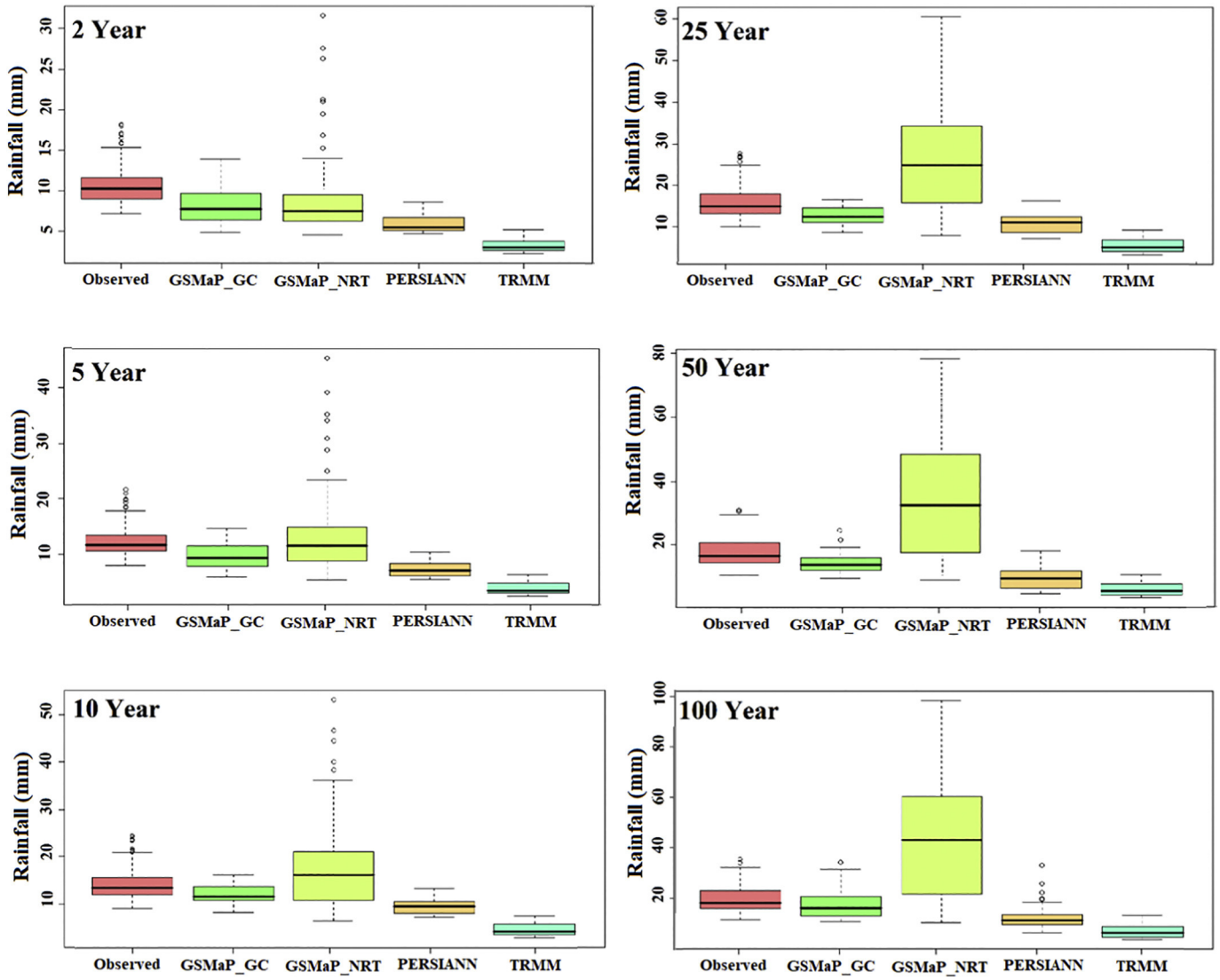

Fig. 9. Rainfall intensity at different return periods estimated using observed and remotely sensed rainfall data.

unable to replicate the observed rainfall, although overall GSMaP performed more effectively than TRMM. Islam (2018) compared six remote sensing products over Bangladesh including PERSIANN, CMORPH, IMERG (non-gauge-calibrated and gauge-calibrated), and GSMaP_NRT and GSMaP-GC. GSMaP_GC performed best, while PERSAINN was the worst performer.

4.2. Fitting PDF and estimation of PDF parameters

An evaluation was conducted on the performance of the four PDFs and four parameter estimators using negative log likelihood goodness-of-fit tests. Annual maximum rainfall amount of 1, 3, 6, 12, 24, 48 and 72 h durations for the PDFs and parameter estimation methods were assessed at all eighty stations. Log-likelihood estimates for one location in the southern peninsular (station Johor 2,025,001) are presented in Table 2. The GEV distribution and MLE estimator provided the lowest log-likelihood estimates for rainfall amount of all durations. No significant variation was observed in the log-likelihood estimates for MLE, GMLE and L-moment approaches. For most of the cases MLE provided the least likelihood values for estimating the distribution parameters.

The best PDF and parameter estimator of rainfall of different duration is shown in Fig. 6. Results revealed that GEV is the most suitable PDF with MLE and the best parameter estimation method at most of the stations. The GEV distribution with MLE estimator provided the least log-likelihood estimates at 62% of the stations, followed by GEV with a GMLE estimator at 14% of the stations. The GP distribution with MLE is at 11%, Exponential with MLE is at 5%, GEV with L-moments is at 4% and Gubmle with MLE is at 4% of the stations. Therefore, the rainfall properties were fitted with GEV and the distribution parameters were estimated using the MLE method for the generation of the IDF curves.

Based on the goodness of fit test, most suitable PDF was selected using the annual maximum of observed rainfall data in this work. The PDF selected was fitted to annual maximum of both observed and remote sensing rainfall data for developing IDF curves for observed and remote sensing data. Therefore, it is suggested to compare various PDFs separately for developing remote sensing IDF curves in the future.

4.3. Development of IDF curves

IDF curves were developed using both hourly observed and satellite rainfall data for the period 2000–2018 at all 80 stations. The curves of Pahang station (ID: 3628001), which is located in the central region of the Peninsula, are shown in Fig. 7. The y-axis represents rainfall intensity (in mm/h) and the x-axis indicates duration (in hours). IDF curves for different return periods are also presented. An increase in

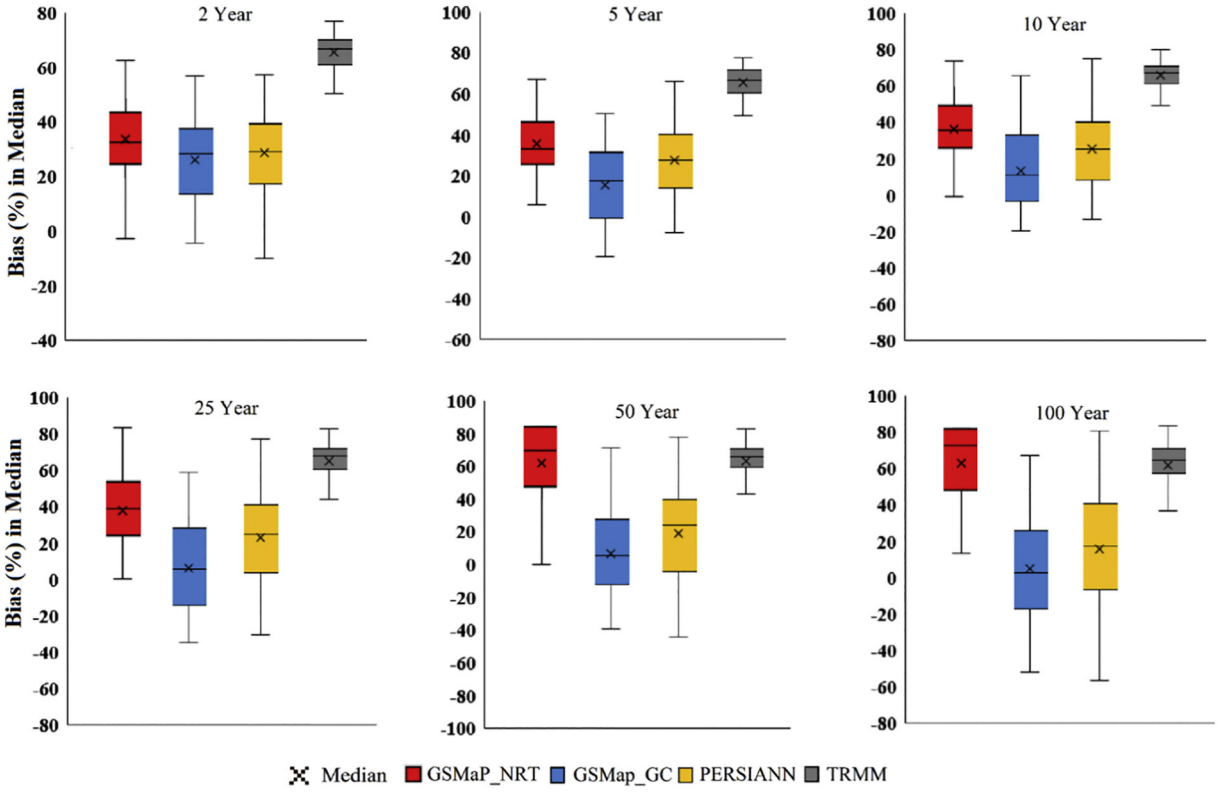

Fig. 10. Percent of bias in median intensity of remote sensing rainfall for different return periods at all stations.

rainfall intensity with different return periods and a decrease in rainfall intensity with duration is noted (Fig. 7). The result of one station is shown as an example.

4.4. Assessing the performance of remotely-sensed products

IDF curves, developed using both remotely sensed and observed rainfall data, were compared in order to estimate the bias in the IDF curves generated using the satellite-derived rainfall. The bias in median rainfall intensity for all durations was estimated. The bias of different remote sensing precipitation products was then used to rank the products at the different stations. The remote sensing precipitation data which best replicated the observed IDF curves is presented in Fig. 8. The best precipitation product for estimating IDF curves was found to be GSMaP_GC (at 51 of the 80 stations, or 66%), followed by GSMaP_NRT (34%). The PERSIAN and TRMM_3H42V7 products did not perform well at any of the locations. In Fig. 8 shows locations at which GSMaP_GC ranked 1st (blue) and at which GSMP_GC ranked 2nd (yellow). GSMaP_GC performed next to GSMaP_NRT at the locations, where GSMaP_NRT performed best. Similarly, GSMaP_NRT performed next to GSMaP_GC at the locations, where GSMaP_GC was found to perform best. The TRMM_3B42V7 product showed a high bias in its IDF curves.

The performance of IDF curves estimated using remote sensing precipitation was assessed by comparing them with IDF curves estimated using the observed rainfall. Rainfall intensity for different return periods using the observed and remote sensing precipitation data are presented in Fig. 9. The results show that rainfall intensity for different duration estimated using GSMaP_GC was most similar to in-situ rainfall intensity for all return periods. A large difference was observed between GSMaP_NRT and the observed rainfall intensity for all the return periods (except for the 2-year period). GSMaP_NRT was found to overestimate the rainfall intensity for ≥10-year return periods. PERSIANN and TRMM appeared to underestimate rainfall intensity for all return periods. Previous studies have also reported an underestimation of high rainfall using remote sensing precipitation products (Hur et al., 2018; Sharifi et al., 2019; Peng et al., 2020; Yao et al., 2020; Liu et al., 2019; Mahmoud et al., 2019).

The percentage of bias in the median rainfall intensity for different durations at all locations were calculated and are presented in Fig. 10. The figures clearly show that all of the remote sensing precipitation data underestimated rainfall intensity of all durations, with the exception of GSMaP_NRT for the higher return periods (> 10-year). GSMaP_GC was found to be the best performer, (underestimating by 8–27%) followed by PERSIANN (28–32%) and GSMaP_NRT (35–49%). The underestimation was highest for TRMM_3B42V7 (65–67%). Bias in GSMaP_GC was found to be less (8–12%) for the higher return periods (> 10-year) and also high for the lower return periods (18–27%). The bias in other rainfall product was consistently high for all return periods.

It has been reported that most of the remote sensing precipitation products overestimate light rainfall and underestimate high rainfall (Sharifi et al., 2019, Peng et al., 2020, Yao et al., 2020, Liu et al., 2019, Mahmoud et al., 2019). This causes a high bias in IDF curve estimated using remote sensing precipitation data. Sun et al. (2019) used remote sensing rainfall for developing IDF curves in Singapore and reported 70% bias in remote sensing based IDF curves compared to observed IDF curves. Ombadi et al. (2018) evaluated the performance of PERSIANN-CDR against NOAA Atlas 14 for estimating IDF curves in the USA, with results showing a median bias of between 3 and 22% for precipitation durations of one to three days.

Rainfall intensity for different durations at all stations was used to evaluate individual performances using a Taylor diagram (Taylor, 2001). The results are presented in Fig. 11. The circle in black located on the x-axis represents the observed rainfall while filled circles with different colours denote precipitation based on remote sensing products. The diagram shows the performance of datasets based on similarity in correlation and variability. The circle nearest to the observed

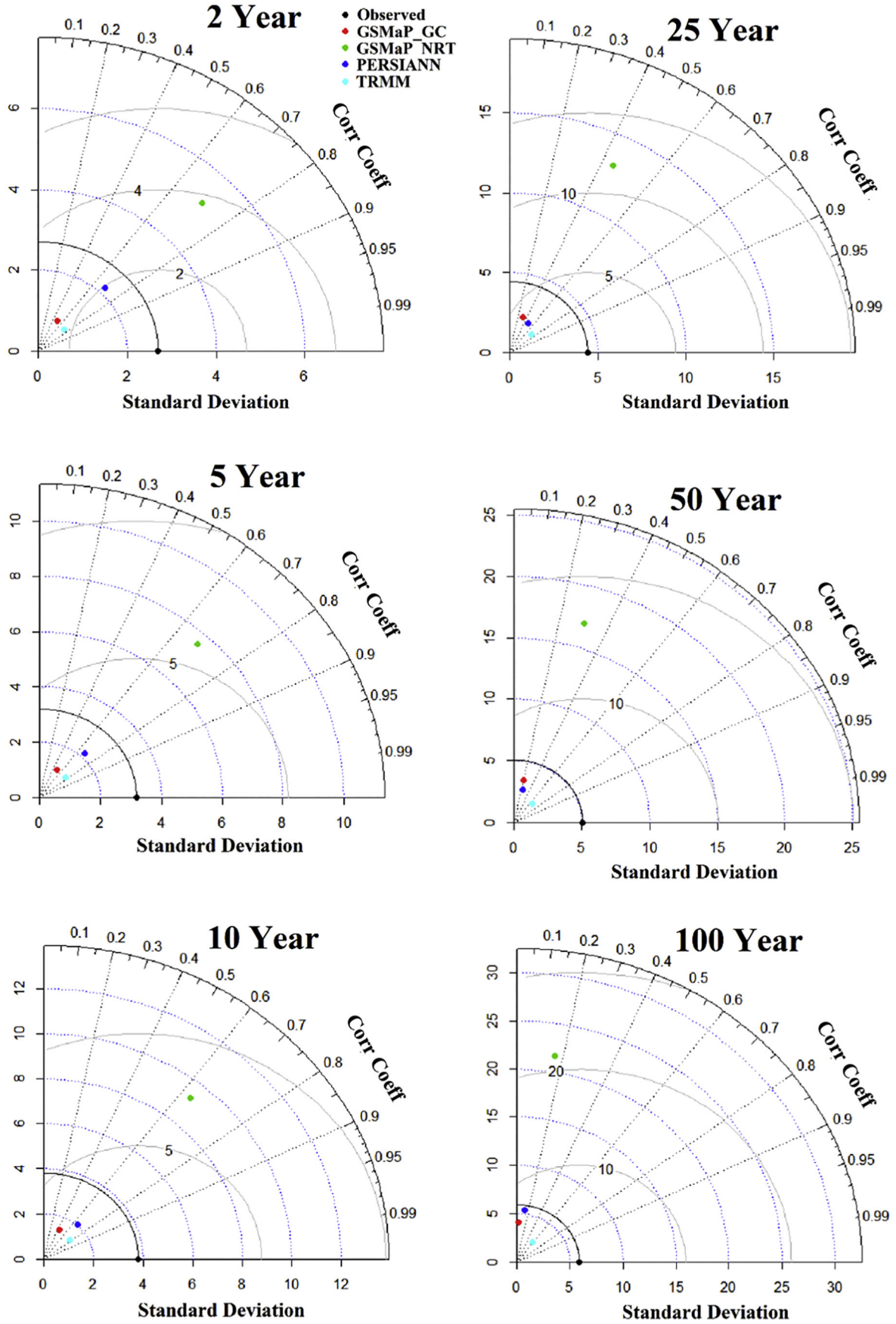

Fig. 11. Taylor diagram, showing performance of different remote sensing rainfall products in replicating observed rainfall intensity at different return periods.

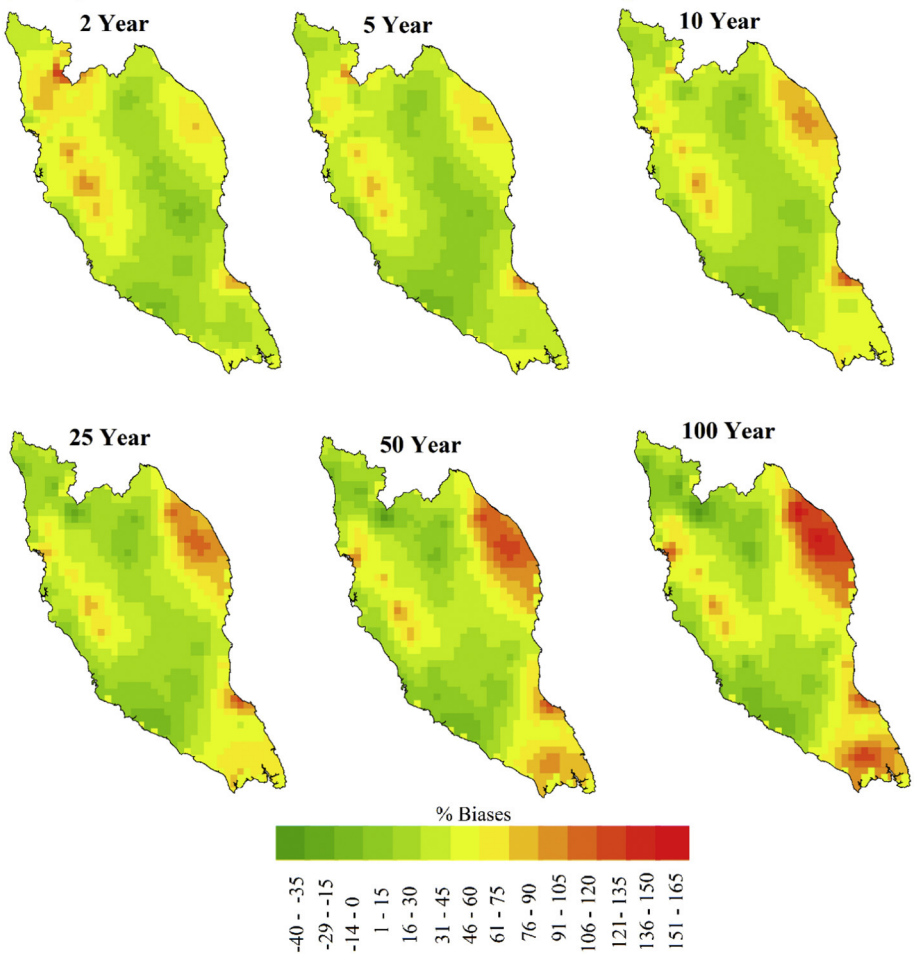

Fig. 12. Spatial distribution of bias in GSMaP_CG rainfall intensity for different return periods.

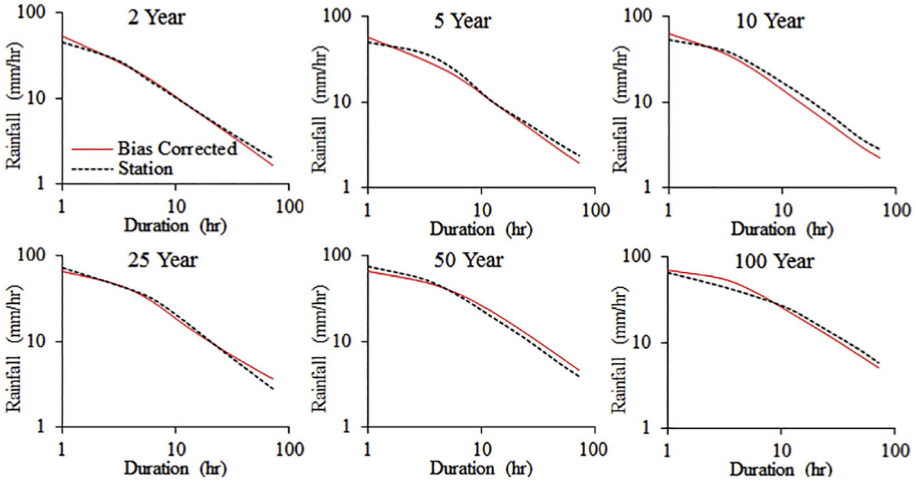

Fig. 13. Observed and bias-corrected GSMaP_CG IDF curves for different return periods of a station located in the south of the Peninsula.

one represents the best product. The analysis shows good performance of the GSMaP_GC rainfall product for lower return periods (< 10-year), with an almost similar performance for higher return periods.

A gradual decrease in correlation with return period was observed. This is mainly due to a higher bias in the rainfall intensity of the higher return periods. Similar results were also found by when comparing radar and satellite (CMORPH) IDF curves in the East Mediterranean region; specifically a high correlation for shorter return period, and then a gradual decrease in correlation with increasing return periods.

The study revealed a high bias in the IDF curves which were estimated using the remote sensing data, with the least bias being shown by GSMaP_GC. The bias in GSMaP_GC for return periods > 10-year was 8–12%, while it was a bit higher for the lower return periods (18–27%). This indicates that GSMaP_GC rainfall can be used for generating IDF curves once the small amount of bias has been corrected. The study revealed that the good performance of remote sensing rainfall data in

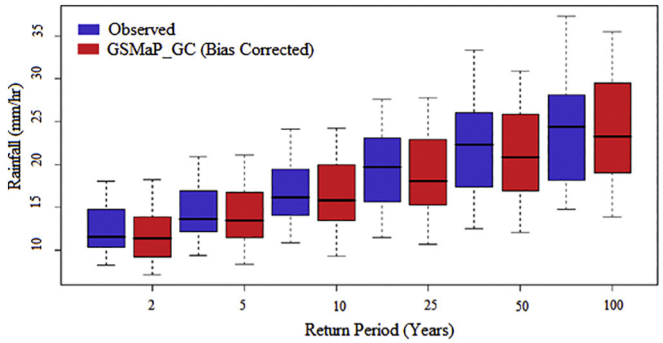

Fig. 14. Observed and GSMaP_GC rainfall intensity after bias-correction for different return periods.

terms of their ability to replicate annual or seasonal rainfall totals, or the actual spatial distribution of rainfall, does not mean that this data can be used to provide a better estimation of the IDF curves. The reliability of the remote sensing rainfall data should be based on their ability to reproduce reliable observed IDF curves.

4.5. Spatial distribution of bias

Sixty-four of the 80 stations (80% stations) were randomly selected for estimation of the spatial distribution of bias in GSMaP_GC rainfall intensity for differing return periods. The remaining 16 stations (20% of the total) were used to assess the performance of the bias-corrected IDF curves at defined ungauged locations. Though the bias in the median was less for higher return periods and high for lower return periods, the spatial variability of bias was reduced for the lower return periods and increased for the higher return periods (Fig. 12). The bias was found to be higher in the coastal areas and lower in the central region. The highest bias in rainfall intensity for all return periods was found in the northeast. Rainfall intensity in this region is high compared to other regions. As the GSMaP_GC rainfall failed to capture the high rainfall intensity, the bias is therefore very high.

The biases in remote sensing rainfall data depend on various physiographic factors. This includes topography, elevation and proximity to shorelines, as well as climatic factors such as wind speed and cloud cover type (Yao et al., 2020; Kalimeris and Kolios, 2019; Cavalcante et al., 2020; Sobral et al., 2020). Future studies should concentrate on correlating specific physiographic and climatic factors with the noted bias in remote sensed rainfall in order to better understand the various factors affecting the bias. These factors can then be incorporated into a bias correction process to provide a better estimation of IDF curves generated from remotely sensed precipitation products.

4.6. Performance bias corrected IDF curves

Bias estimates for the 16 stations not used to estimate the spatial distribution of bias (Fig. 12) were used to assess the performance of the bias-corrected GSMaP_GC IDF curves at ungauged locations. An example of the evaluation results for the observed and bias-corrected GSMaP_CG IDF curves for different return periods of a station located in the south of the peninsula (Johor 2,025,001) are shown in Fig. 13. This shows a good match between observed and bias-corrected GSMaP_GC IDF curves for the different return periods. The graphed results are presented in Fig. 14, showing a perfect match in rainfall intensity between observed and GSMaP_GC data. The respective median values agree well for the lower return periods (< 10-year). The bias in the median of the rainfall intensity of GSMaP_GC for the higher return periods was also found to be very close to the intensity of the observed rainfall and the range of rainfall intensity for the different return periods was also found to match well. These results indicate that the bias-corrected IDF curves derived from GCMaP_GC rainfall are eminently suitable for hydrological studies and hydraulic design work.

5. Conclusion

In a study, four satellite-derived rainfall data products were evaluated to determine their ability to replicate IDF curves in Ppeninsular Malaysia. An analysis of the initial results indicated that all the remote sensing rainfall underestimated the rainfall intensities for different durations and return periods. When the results were corrected for bias, however, the outcomes looked more promising. This shows that the correction for bias is essential when generating IDF curves using remote sensing precipitation data. The results indicate that GSMaP_GC is the best product to use for the IDF curves (with an 8–27% bias). The spatial distribution of bias for different rainfall return periods for GSMaP_GC was also generated in this study, and can be used for correction of bias in the IDF curves estimated using GSMaP_GC. This enables use at locations where actual rainfall data is not available and so the procedure used in this study can be used to develop IDF curves in any regions where suitable data is lacking. These study results can be used when designing hydraulic structures in the regions of Peninsular Malaysia where gauged data are unavailable. Biases in remote sensing data can be corrected before being use in IDF curve development and compared with the results obtained in this study. The performance of different bias correction methods can be evaluated to improve the performance of remote sensing rainfall in generating IDF curves. The best PDFs can be estimated for both observed and remote sensing data when preparing corresponding IDF curves to allow a better comparison with remote sensing rainfall products. The performance of remote sensing data based on different rainfall extremes such as intensity, duration and frequency can also be evaluated. Besides, the performance of other high-resolution satellite-based rainfall products that offer data for shorter period can be compared and evaluated.

Declaration of Competing Interest

None.

Acknowledgements

The authors are grateful to Universiti Teknologi Malaysia (UTM) for providing financial support to conduct this study through Grant No. 01M96

References

Abbaspour, K.C., Rouholahnejad, E., Vaghefi, S., Srinivasan, R., Yang, H., Kløve, B., 2015. A continental-scale hydrology and water quality model for Europe: Calibration and uncertainty of a high-resolution large-scale SWAT model. J. Hydrol. 524, 733–752.

Ahmed, K., Shahid, S., Ismail, T., Nawaz, N., Wang, X.J., 2019. Absolute homogeneity assessment of precipitation time series in an arid region of Pakistan. Atmósfera 31 (3), 301–316.

Al-Amri, N.S., Subyani, A.M., 2017. Generation of rainfall intensity duration frequency (IDF) curves for ungauged sites in arid region. Earth Syst. Environ. 1, 8.

Alijanian, M., Rakhshandehroo, G.R., Mishra, A.K., Dehghani, M., 2017. Evaluation of satellite rainfall climatology using CMORPH, PERSIANN-CDR, PERSIANN, TRMM, MSWEP over Iran. Int. J. Climatol. https://doi.org/10.1002/Joc.5131.

Almazroui, M., Saeed, S., 2020. Contribution of extreme daily precipitation to total rainfall over the Arabian Peninsula. Atmos. Res. 231, 104672.

Almazroui, M., Şen, Z., Mohorji, A.M., et al., 2019. Impacts of climate change on water engineering structures in arid regions: case studies in Turkey and Saudi Arabia. Earth Syst. Environ. 3, 43–57. 2019. https://doi.org/10.1007/s41748-018-0082-6.

Belo-Pereira, M., Dutra, E., Viterbo, P., 2011. Evaluation of global precipitation data sets over the Iberian Peninsula. J. Geophys. Res.-Atmos. 116.

Bierman, G., Belzer, M.R., Vandergraft, J.S., Portert, D., 1989. Maximum likelihood estimation using square root information filters. In: American Control Conference, 1989. IEEE, pp. 2646–2652.

Bosman, P.A., Thierens, D., 2000. Negative Log-Likelihood and Statistical Hypothesis Testing as the Basis of Model Selection in IDEAs.

Cavalcante, R.B.L., Da Silva Ferreira, D.B., Pontes, P.R.M., Tedeschi, R.G., Da Costa, C.P.W., De Souza, E.B., 2020. Evaluation of extreme rainfall indices from CHIRPS precipitation estimates over the Brazilian Amazonia. Atmos. Res. 238, 104879.

Chen, F., Li, X., 2016. Evaluation of IMERG and TRMM 3B43 monthly precipitation products over mainland China. Remote Sens. 8, 472.
Chen, S., Hong, Y., Cao, Q., Kirstetter, P.-E., Gourley, J.J., Qi, Y., Zhang, J., Howard, K., HU, J., Wang, J., 2013. Performance evaluation of radar and satellite rainfalls for Typhoon Morakot over Taiwan: are remote-sensing products ready for gauge denial scenario of extreme events? J. Hydrol. 506, 4–13.
Chow, V.T., Maidment, D.R., Mays, L.W., 1988. Applied Hydrology.
Courty, L.G., Wilby, R.L., Hillier, J.K., Slater, L.J., 2019. Intensity-duration-frequency curves at the global scale. Environ. Res. Lett. 14, 084045.
De Paola, F., Giugni, M., Topa, M.E., Bucchignani, E., 2014. Intensity-Duration-Frequency (IDF) Rainfall Curves, for Data Series and Climate Projection in African cities. 3. SpringerPlus, pp. 133.
Dewan, A., Hu, K., Kamruzzaman, M., Uddin, M.R., 2019. Evaluating the spatiotemporal pattern of concentration, aggressiveness and seasonality of precipitation over Bangladesh with time–series tropical rainfall measuring Mission data. In: Extreme Hydroclimatic Events and Multivariate Hazards in a Changing Environment. Elsevier.
Endreny, T.A., Imbeah, N., 2009. Generating robust rainfall intensity–duration–frequency estimates with short-record satellite data. J. Hydrol. 371, 182–191.
Faiz, M.A., Liu, D., Fu, Q., Sun, Q., Li, M., Baig, F., Li, T., Cui, S., 2018. How accurate are the performances of gridded precipitation data products over Northeast China? Atmos. Res. 211, 12–20.
Fienberg, S.E., 1997. Introduction to RA Fisher on inverse probability and likelihood. Stat. Sci. 12, 161.
Fisher, R., 1912. The Maximum–Likelihood–Method. Messenger in Mathematics. vol. 41. pp. 155–160.
Giarno, M.P.H., 2018. Distribution of Accuracy of TRMM Daily Rainfall in Makassar Strait. Forum Geografi 32 (1), 38–52.
Hajani, E., Rahman, A., Ishak, E., 2017. Trends in extreme rainfall in the state of New South Wales, Australia. Hydrol. Sci. J. 62, 2160–2174.
Hasan, E., Tarhule, A., Hong, Y., Moore, B., 2019. Assessment of physical water scarcity in Africa using GRACE and TRMM satellite data. Remote Sens. 11, 904.
Herrera, S., Gutiérrez, J.M., Ancell, R., Pons, M., Frías, M., Fernández, J., 2012. Development and analysis of a 50-year high-resolution daily gridded precipitation dataset over Spain (Spain02). Int. J. Climatol. 32, 74–85.
Hilbe, J.M., Robinson, A.P., 2013. Methods of Statistical Model Estimation. CRC Press.
Hong, H.P., Li, S.H., Mara, T.G., 2013. Performance of the generalized least-squares method for the Gumbel distribution and its application to annual maximum wind speeds. J. Wind Eng. Ind. Aerodyn. 119, 121–132.
Hosking, J.R.M., 1990. The Theory of Probability Weighted Moments, Research Report RC12210. IBM Thomas J. Watson Research Center, Yorktown Heights, NY.
Hosking, J.R.M., 1990. L-moments: Analysis and Estimation of Distribution Using Linear Combination of Order Statistics. J. R. Stat. Soc., Set. B 52 (1), 105–124.
Huang, W.-R., Chang, Y.-H., Liu, P.-Y., 2018. Assessment of IMERG precipitation over Taiwan at multiple timescales. Atmos. Res. 214, 239–249.
Huffman, G.J., 2016. The Transition in Multi-Satellite Products from TRMM to GPM (TMPA to IMERG). Version 161025, 5.
Hur, J., Raghavan, S.V., Nguyen, N.S., Liong, S.Y., 2018. Are satellite products good proxies for gauge precipitation over Singapore? Theor Appl Climatol 132, 921–932. https://doi.org/10.1007/s00704-017-2132-7.
IPCC, 2014. In: Pachauri, R.K., Meyer, L.A. (Eds.), IPCC, 2014: Climate Change 2014: Synthesis Report. Contribution of Working Groups I, II and III to the Fifth Assessment Report of the Intergovernmental Panel on Climate Change Core Writing Team. IPCC, Geneva, Switzerland (151 pp). https://www.ipcc.ch/report/ar5/syr/.
Islam, M.A., 2018. Statistical comparison of satellite-retrieved precipitation products with rain gauge observations over Bangladesh. Int. J. Remote Sens. 39, 2906–2936.
Jenkinson, A.F., 1955. The frequency distribution of the annual maximum (or minimum) values of meteorological elements. Q. J. R. Meteorol. Soc. 81, 158–171.
Jiang, S., Ren, L., Zhou, M., Yong, B., Zhang, Y., Ma, M., 2017. Drought monitoring and reliability evaluation of the latest TMPA precipitation data in the Weihe River Basin, Northwest China. J. Arid Land 9, 256–269.
Kalimeris, A., Kolios, S., 2019. TRMM-based rainfall variability over the Central Mediterranean and its relationships with atmospheric and oceanic climatic modes. Atmos. Res. 230, 104649.
Khan, N., Pour, S.H., Shahid, S., Ismail, T., Ahmed, K., Chung, E.S., Nawaz, N., Wang, X., 2019. Spatial distribution of secular trends in rainfall indices of peninsular Malaysia in the presence of long-term persistence. Meteorl. Appl. https://doi.org/10.1002/met.1792.
Kidd, C., Becker, A., Huffman, G.J., Muller, C.L., Joe, P., Skofronick-Jackson, G., Kirschbaum, D.B., 2017. So, how much of the Earth's surface is covered by rain gauges? Bull. Am. Meteorol. Soc. 98, 69–78.
Kjeldsen, T.R., Lundorf, A., Rosbjerg, D., 2000. Use of a two-component exponential distribution in partial duration modelling of hydrological droughts in Zimbabwean rivers. Hydrol. Sci. J. 45 (2), 285–298.
Koutsoyiannis, D., Kozonis, D., Manetas, A., 1998. A mathematical framework for studying rainfall intensity-duration-frequency relationships. J. Hydrol. 206, 118–135.
Kumar, B., Lakshmi, V., 2018. Accessing the capability of TRMM 3B42 V7 to simulate streamflow during extreme rain events: Case study for a Himalayan River Basin. J. Earth Syst. Sci. 127, 27.
Laiti, L., Mallucci, S., Piccolroaz, S., Bellin, A., Zardi, D., Fiori, A., Nikulin, G., Majone, B., 2018. Testing the hydrological coherence of high-resolution gridded precipitation and temperature data sets. Water Resour. Res. 54, 1999–2016.
Liew, S.C., Raghavan, S.V., Liong, S.-Y., 2014. Development of Intensity-Duration-Frequency curves at ungauged sites: risk management under changing climate. Geosci. Lett. 1, 8.
Lima, C.H., Kwon, H.-H., Kim, Y.-T., 2018. A local-regional scaling-invariant Bayesian GEV model for estimating rainfall IDF curves in a future climate. J. Hydrol. 566, 73–88.
Liu, J., Shangguan, D., Liu, S., Ding, Y., Wang, S., Wang, X., 2019. Evaluation and comparison of CHIRPS and MSWEP daily-precipitation products in the Qinghai-Tibet Plateau during the period of 1981–2015. Atmos. Res. 230, 104634.
Mahmoud, M.T., Hamouda, M.A., Mohamed, M.M., 2019. Spatiotemporal evaluation of the GPM satellite precipitation products over the United Arab Emirates. Atmos. Res. 219, 200–212.
Marra, F., Nikolopoulos, E., Creutin, J., Borga, M., 2016. Space–time organization of debris flows-triggering rainfall and its effect on the identification of the rainfall threshold relationship. J. Hydrol. 541, 246–255.
Martins, E.S., Stedinger, J.R., 2000. Generalized maximum-likelihood generalized extreme-value quantile estimators for hydrologic data. Water Resour. Res. 36 (3), 737–744.
Mayowa, O.O., Pour, S.H., Shahid, S., Mohsenipour, M., Harun, S.B., Heryansyah, A., Ismail, T., 2015. Trends in rainfall and rainfall-related extremes in the east coast of peninsular Malaysia. J. Earth Syst. Sci. 124, 1609–1622.
Mission, T.R.M., 2011. TRMM (TMPA) Rainfall Estimate L3 3 hour 0.25 degree x 0.25 degree V7, Greenbelt, MD, Goddard Earth Sciences Data and Information Services Center (GES DISC). TRMM_3B42_7. html.
Nashwan, M., Shahid, S., 2019a. Spatial distribution of unidirectional trends in climate and weather extremes in Nile river basin. Theor. Appl. Climatol. 137, 1181–1199.
Nashwan, M.S., Shahid, S., 2019b. Symmetrical uncertainty and random forest for the evaluation of gridded precipitation and temperature data. Atmos. Res. 230, 104632.
Nashwan, M., Shahid, S., Chung, E.-S., Ahmed, K., Song, Y., 2018. Development of climate-based index for hydrologic hazard susceptibility. Sustainability 10, 2182.
Nashwan, M.S., Shahid, S., Rahim, N.A., 2019. Unidirectional trends in annual and seasonal climate and extremes in Egypt. Theor. Appl. Climatol. 136, 457–473.
Nguyen, P., Ombadi, M., Sorooshian, S., Hsu, K., Aghakouchak, A., Braithwaite, D., Ashouri, H., Thorstensen, A.R., 2018. The PERSIANN family of global satellite precipitation data: a review and evaluation of products. Hydrol. Earth Syst. Sci. 22, 5801–5816.
Noor, M., Ismail, T., Shahid, S., Nashwan, M.S., Ullah, S., 2019. Development of multimodel ensemble for projection of extreme rainfall events in Peninsular Malaysia. Hydrol. Res. 50, 1772–1788.
Okamoto, K.I., Ushio, T., Iguchi, T., Takahashi, N., Iwanami, K., 2005. The Global Satellite Mapping of Precipitation (GSMaP) Project.
Ombadi, M., Nguyen, P., Sorooshian, S., hsu, K.L., 2018. Developing intensity-duration-frequency (IDF) curves from satellite-based precipitation: methodology and evaluation. Water Resour. Res. 54, 7752–7766.
Overeem, A., Buishand, T., Holleman, I., 2009. Extreme rainfall analysis and estimation of depth-duration-frequency curves using weather radar. Water Resour. Res. 45.
Palomino-Ángel, S., Anaya-Acevedo, J.A., Botero, B.A., 2019. Evaluation of 3B42V7 and IMERG daily-precipitation products for a very high-precipitation region in northwestern South America. Atmos. Res. 217, 37–48.
Panziera, L., Gabella, M., Zanini, S., Hering, A., Germann, U., Berne, A., 2016. A radar-based regional extreme rainfall analysis to derive the thresholds for a novel automatic alert system in Switzerland. Hydrol. Earth Syst. Sci. 20, 2317–2332.
Peleg, N., Marra, F., Fatichi, S., Paschalis, A., Molnar, P., BURLANDO, P., 2018. Spatial variability of extreme rainfall at radar subpixel scale. J. Hydrol. 556, 922–933.
Peng, J., Dadson, S., Hirpa, F., Dyer, E., Lees, T., Gonzalez Miralles, D., Vicente-serrano, S.M., Funk, C., 2020. A pan-African high-resolution drought index dataset. Earth Syst. Sci. Data 12, 753–769.
Poudel, K.P., Cao, Q.V., 2013. Evaluation of methods to predict Weibull parameters for characterizing diameter distributions. For. Sci. 59, 243–252.
Pour, S.H., Harun, S., Shahid, S., 2014. Genetic programming for the downscaling of extreme rainfall events on the east coast of peninsular malaysia. Atmosphere 2014 (5), 914–936.
Pour, S.H., Wahab, A.K.A., Shahid, S., Ismail, Z.B., 2020a. Changes in reference evapotranspiration and its driving factors in peninsular Malaysia. Atmos. Res. 249, 105096. https://doi.org/10.1016/j.atmosres.2020.105096.
Pour, S.H., Wahab, A.K.A., Shahid, S., Asaduzzaman, M., Dewan, A., 2020b. Low impact development techniques to mitigate the impacts of climate-change-induced urban floods: current trends, issues and challenges. Sustain. Cities Soc. 62, 102373. https://doi.org/10.1016/J.SCS.2020.102373.
Pour, S.H., Wahab, A.K.A., Shahid, S., 2020c. Physical-empirical models for prediction of seasonal rainfall extremes of Peninsular Malaysia. Atmos. Res. 233, 104720. https://doi.org/10.1016/j.atmosres.2019.104720.
Pour, S.H., Wahab, A.K.A., Shahid, S., 2020d. Spatiotemporal changes in precipitation indicators related to bioclimate in Iran. Theor. Appl. Climatol. https://doi.org/10.1007/s00704-020-03192-6.
Prakash, S., Mitra, A.K., Momin, I.M., Rajagopal, E.N., Basu, S., Collins, M., Turner, A.G., Achuta Rao, K., Ashok, K., 2015. Seasonal intercomparison of observational rainfall datasets over India during the southwest monsoon season. Int. J. Climatol. 35, 2326–2338.
Prein, A.F., Gobiet, A., 2017. Impacts of uncertainties in European gridded precipitation observations on regional climate analysis. Int. J. Climatol. 37, 305–327.
Rahman, A.S., Rahman, A., Zaman, M.A., Haddad, K., Ahsan, A., Imteaz, M., 2013. A study on selection of probability distributions for at-site flood frequency analysis in Australia. Nat. Hazards 69, 1803–1813.
Reis Jr., D.S., Stedinger, J.R., 2005. Bayesian MCMC flood frequency analysis with historical information. J. Hydrol. 313 (1–2), 97–116.
Schiemann, R., Liniger, M., Frei, C., 2010. Reduced space optimal interpolation of daily rain gauge precipitation in Switzerland. J. Geophys. Res.-Atmos. 115.
Şen, Z., 2019. Annual daily maximum rainfall-based IDF curve derivation methodology. Earth Syst. Environ. 3, 463–469. https://doi.org/10.1007/s41748-019-00124-x.
Serrat-Capdevila, A., Merino, M., Valdes, J.B., Durcik, M., 2016. Evaluation of the

performance of three satellite precipitation products over Africa. Remote Sens. 8, 836.
Shahid, S., Pour, S.H., Wang, X.-J., et al., 2017. Impacts and adaptation to climate change in Malaysian real estate. Int. J. Climat. Chang. Strateg. Manage. 9 (1), 87–103. https://doi.org/10.1108/IJCCSM-01-2016-0001.
Sharifi, E., Eitzinger, J., Dorigo, W., 2019. Performance of the State-Of-The-Art Gridded Precipitation Products over Mountainous Terrain: a Regional Study over Austria. Remote Sens. 11, 2018.
Sobral, B.S., De Oliveira-Júnior, J.F., Alecrim, F., Gois, G., Muniz-Júnior, J.G., De Bodas Terassi, P.M., Pereira-Júnior, E.R., Lyra, G.B., Zeri, M., 2020. PERSIANN-CDR based characterization and trend analysis of annual rainfall in Rio De Janeiro State, Brazil. Atmos. Res. 238, 104873.
Sorooshian, S., Aghakouchak, A., Arkin, P., Eylander, J., Foufoula-Georgiou, E., Harmon, R., Hendrickx, J.M., Imam, B., Kuligowski, R., Skahill, B., 2011. Advancing the remote sensing of precipitation. Bull. Am. Meteorol. Soc. 92, 1271–1272.
Sun, Y., Wendi, D., Kim, D.E., Liong, S.-Y., 2019. Deriving intensity–duration–frequency (IDF) curves using downscaled in situ rainfall assimilated with remote sensing data. Geosci. Lett. 6, 17.
Tan, M.L., Duan, Z., 2017. Assessment of GPM and TRMM precipitation products over Singapore. Remote Sens. 9, 720.
Tan, M.L., Ibrahim, A.L., Duan, Z., Cracknell, A.P., Chaplot, V., 2015. Evaluation of six high-resolution satellite and ground-based precipitation products over malaysia. Remote Sens. 7, 1504–1528. https://doi.org/10.3390/Rs70201504.
Taylor, K.E., 2001. Summarizing multiple aspects of model performance in a single diagram. J. Geophys. Res.-Atmos. 106, 7183–7192.
Tien Thanh, N., Dutto Aldo Remo, L., 2018. Projected changes of precipitation idf curves for short duration under climate change in Central Vietnam. Hydrology 5, 33.
Trenberth, K.E., 2011. Changes in precipitation with climate change. Clim. Res. 47, 123–138.
Ushio, T., Sasashige, K., Kubota, T., Shige, S., Okamoto, K.I., Aonashi, K., Inoue, T., Takahashi, N., Iguchi, T., Kachi, M., 2009. A Kalman filter approach to the Global Satellite Mapping of Precipitation (GSMaP) from combined passive microwave and infrared radiometric data. J. Meteorol. Soc. Japan. Ser. II 87, 137–151.
Wang, X.-J., Zhang, J.-Y., Shahid, S., et al., 2016. Adaptation to climate change impacts on water demand. Mitig. Adapt. Strateg. Glob. Chang. 21 (1), 81–99.
Watt, E., Marsalek, J., 2013. Critical review of the evolution of the design storm event concept. Can. J. Civ. Eng. 40, 105–113.
Willems, P., 2000. Compound intensity/duration/frequency-relationships of extreme precipitation for two seasons and two storm types. J. Hydrol. 233, 189–205.
Wright, D.B., Smith, J.A., Villarini, G., Baeck, M.L., 2013. Estimating the frequency of extreme rainfall using weather radar and stochastic storm transposition. J. Hydrol. 488, 150–165.
Yang, Y., Wang, G., Wang, L., Yu, J., Xu, Z., 2014. Evaluation of Gridded Precipitation Data for Driving SWAT Model in Area Upstream of Three Gorges Reservoir.
Yang, P., Xia, J., Zhang, Y., Zhan, C., Qiao, Y., 2018. Comprehensive assessment of drought risk in the arid region of Northwest China based on the global palmer drought severity index gridded data. Sci. Total Environ. 627, 951–962.
Yao, J., Chen, Y., Yu, X., Zhao, Y., Guan, X., Yang, L., 2020. Evaluation of multiple gridded precipitation datasets for the arid region of Northwestern China. Atmos. Res. 236, 104818.
Yatagai, A., Arakawa, O., Kamiguchi, K., Kawamoto, H., Nodzu, M.I., Hamada, A., 2009. A 44-year daily gridded precipitation dataset for Asia based on a dense network of rain gauges. Sola 5, 137–140.
Yuan, F., Zhang, L., Soe, K.M.W., Ren, L., Zhao, C., Zhu, Y., Jiang, S., Liu, Y., 2019. Applications of TRMM-and GPM-era multiple-satellite precipitation products for flood simulations at sub-daily scales in a sparsely gauged watershed in Myanmar. Remote Sens. 11, 140.
Yue, S., Wang, C.Y., 2004. A comparison of two bivariate extreme value distributions. Stoch. Env. Res. Risk A. 18, 61–66.
Zad, M., Najja, S., Zulkafli, Z., Muharram, F.M., 2018. Satellite rainfall (TRMM 3B42-V7) performance assessment and adjustment over Pahang River Basin, Malaysia. Remote Sens. 10, 388.
Zhu, D., Yao, H., Jiang, B., Yu, P., 2018. Negative log likelihood ratio loss for deep neural network classification. arXiv 1–4 preprint arXiv:1804.10690.
Zhu, B., Chen, J., Chen, H., 2019. Performance of multiple probability distributions in generating daily precipitation for the simulation of hydrological extremes. Stoch. Env. Res. Risk A. 33 (8–9), 1581–1592.